Nanoscale

PAPER

View Article Online
View Journal

Cite this: DOI: 10.1039/c5nr02215k

Bimetallic PdAg nanoparticle arrays from monolayer films of diblock copolymer micelles

E. Ehret,*[a] E. Beyou,[b] G. V. Mamontov,[c] T. A. Bugrova,[c] S. Prakash,[a] M. Aouine,[a] B. Domenichini[d] and F. J. Cadete Santos Aires[a,c]

Received 7th April 2015,
Accepted 25th June 2015

DOI: 10.1039/c5nr02215k

www.rsc.org/nanoscale

The self-assembly technique provides a highly efficient route to generate well-ordered structures on a nanometer scale. In this paper, well-ordered arrays of PdAg alloy nanoparticles on flat substrates with narrow distributions of particle size (6–7 nm) and interparticle spacing (about 60 nm) were synthesized by the block copolymer micelle approach. A home-made PS-*b*-P4VP diblock copolymer was prepared to obtain a micellar structure in toluene. Pd and Ag salts were then successfully loaded in the micellar core of the PS-*b*-P4VP copolymer. A self-assembled monolayer of the loaded micelles was obtained by dipping the flat substrate in the solution. At this stage, the core of the micelles was still loaded with the metal precursor rather than with a metal. Physical and chemical reducing methods were used to reduce the metal salts embedded in the P4VP core into PdAg nanoparticles. HRTEM and EDX indicated that Pd-rich PdAg alloy nanoparticles were synthesized by chemical or physical reduction; UV-visible spectroscopy observations confirmed that metallic PdAg nanoparticles were quickly formed after chemical reduction; XPS measurements revealed that the PdAg alloy nanoparticles were in a metallic state after a short time of exposure to O_2 plasma and after hydrazine reduction.

Introduction

Bimetallic nanoparticles (NPs) display unique properties drastically different from those of the corresponding single-component particles. These properties are assumed to result from both the electronic and structural effects of the bimetallic nanoparticle. As these properties depend also on the preparation conditions, the synthesis of bimetallic nanoparticles with accurately controlled structures and compositions is essential to obtain advanced materials for electronic, magnetic, optical and catalytic applications.

The self-assembly technique provides a highly efficient route to generate well-ordered structures on a nanometer scale. The formation of self-assembled structures from block copolymers has generated significant interest because they offer a wide range of possibilities in terms of architecture, size and chemical composition and allow achieving long-range ordering through microphase separation when the different blocks are chemically immiscible.[1–10] The formation of ordered domains is driven by a balance between entropic and enthalpic forces and chemical bond constraints between the blocks. Self-assembled morphologies of traditional diblock copolymers are of four types: lamellar, spherical, bicontinuous and cylindrical.[11] The ultimate morphology is determined by the degree of polymerization and the relative composition of the different blocks. Besides, the phase behaviour of block copolymers in solution is different from that in the melt due to solvent–monomer and monomer–monomer interactions. Self-assembly of polystyrene-*block*-poly(4-vinylpyridine) amphiphilic block copolymer has been studied extensively with different metals and at different pH values.[12–19]

Over the past few years, the fabrication of nanostructures from self-assembled block copolymer templates has been actively studied.[20,21] One of the applications is to employ block copolymers to generate inorganic NPs.[22–25] In this approach, a block copolymer consisting of a hydrophilic and hydrophobic block is dissolved in a selective solvent such as toluene in order to obtain inverse micelles.[26] The core of such inverse micelles can be loaded with a metal salt ligated by complexation or protonisation to the inner polymer block. The reverse micelles can then be transferred from the solution to the substrate by using, for instance, standard spin or dip-coating techniques. The obtained layer exhibits a high degree of hexagonal order, reflecting the packing of spherical micelles. At this

[a]*Institut de Recherche sur la Catalyse et l'Environnement de Lyon, IRCELYON, CNRS, Université Lyon 1, UMR 5256, 2 avenue Albert Einstein, 69626 Villeurbanne Cedex, France. E-mail: eric.ehret@ircelyon.univ-lyon1.fr*
[b]*Ingénierie des Matériaux Polymères, IMP, CNRS, Université Lyon 1, UMR 5223, 15 boulevard Latarget, 69622 Villeurbanne Cedex, France*
[c]*Laboratory of Catalytic Research, National Research Tomsk State University, 36 Lenina Avenue, 634050 Tomsk, Russia*
[d]*Laboratoire Interdisciplinaire Carnot de Bourgogne, ICB, CNRS, Université de Bourgogne, UMR 6303, 9 Av. A. Savary, 21078 Dijon Cedex, France*

stage, the core of the micelles is still loaded with the metallic precursor rather than with a metal. It was found that the removal of the surrounding polymer as well as the reduction of the metallic precursor to a metal can be accomplished by O_2 plasma,[27] UV ozone,[28] or using the vapour or the solution of the reducing agent.[29]

In the present contribution, 2D ordered arrays of bimetallic PdAg nanoparticles were successfully synthesized *via* the copolymer micelle approach. First, a polystyrene-*b*-poly(4-vinylpyridine) (PS-*b*-P4VP) diblock copolymer was synthesized by nitroxide mediated radical polymerization using an alkoxyamine unimolecular initiator (Styryl-SG1). Intermolecular interactions between the $PdCl_2$ and $AgNO_3$ salts and the P4VP micellar core and formation of nanoparticles from the micellar complex were investigated by various spectroscopic and microscopic characterization. Special focus is laid on the influence of the type of reduction treatments, and the chemical nature and the stability of the nanoparticles.

Experimental

Materials

Silver nitrate ($AgNO_3$) (Aldrich), palladium chloride ($PdCl_2$) (Aldrich), hydrazine monohydrate ($N_2H_4{\cdot}H_2O$) (Aldrich) and anhydrous toluene (Aldrich) are used as received. 4-Vinylpyridine (4VP, Aldrich, 95% purity) is purified by distillation under reduced pressure. Styrene (Acros, 99% purity) is distilled under vacuum before use. The alkoxyamine initiator (styryl-DEPN) is prepared using a procedure described in the literature.[30] Anhydrous methanol (Acros, >99%) and tetrahydrofuran (THF, Sigma-Aldrich, >99%) are used as received.

Substrates

N-doped Si wafers (μChemicals) are cleaned using the three solvents process. Amorphous carbon and SiO_2 films deposited on 200 mesh Cu grids are used for electron microscopy.

Polymerization

Block copolymers of poly(styrene)-*block*-poly(4-vinylpyridine) (PS-*b*-P4VP) are synthesized by means of nitroxide mediated free "living" radical polymerization.

Styrene homopolymerization

In a typical procedure, styryl-DEPN (116.34 mg, 2.92×10^{-1} mmol) is dissolved in styrene (25 g, 24 mmol) and the solution is degassed by four freeze–pump–thaw cycles. The vessel is sealed under vacuum and immersed in an oil bath at 115 °C for 8.5 h.

After polymerization, the reaction mixture is dissolved in THF and the polymer is precipitated in methanol. Then, the recovered product is dried under vacuum. Samples are withdrawn during polymerization at specific time-intervals to follow the polymerization kinetics. The molecular weight and molecular weight distributions are determined by SEC analysis. The monomer conversion (43%) is estimated by ^{1}H NMR analysis by comparing the peak areas of the protons of the monomer and the homopolymer. A PS sample with a polymerization degree of 410 is obtained.

Synthesis of PS-*b*-P4VP diblock copolymers

A well-characterized PS homopolymer synthesized in a first step is used as the macroalkoxyamine initiator of the P4VP block. Typically, the PS macroinitiator (2 g, Mn SEC = 49 920 g mol^{-1}, 0.4×10^{-1} mmol) is dissolved in a mixture of DMF (8 g) and 4-vinylpyridine (2 g, 18.8 mmol). The solution is then degassed by three freeze–pump–thaw cycles, sealed under vacuum, placed in a thermostated oil bath at 115 °C and allowed to react for different reaction times. The resulting copolymers are isolated and characterized as described previously for the PS homopolymer. According to the latter experimental procedure, a PS_{410}-*b*-$P4VP_{62}$ block copolymer is synthesized.

Loading of micelles with metal precursors

0.2 or 0.5 wt% solutions (c = 2 or 5 mg mL^{-1}) of the diblock copolymer PS_{410}-*b*-$P4VP_{62}$ in dry toluene is stirred for 8 h in order to allow the formation of reverse micelles. The precise amount of metal precursor ($PdCl_2$, $AgNO_3$) is added to yield a loading ratio (R) of the P4VP micellar core (the ratio between the number of metal ions and the pyridine unit) of R = 0.4 (R = 0.2 for each salt in the case of PdAg nanoparticles). The solutions are stirred for at least 48 h, allowing the metallic salts adequate time to diffuse into the core of the micelle and to complex with the pyridine groups of PVP. The solutions are filtered through 0.45 μm PTFE syringe filters.

Particle nucleation and reduction

A monolayer of PS_{410}-*b*-$P4VP_{62}$ micelles with the metallic salts was dip-coated (typically at 40 mm min^{-1}) using a KSV dip-coater on the Si substrate. At this stage, the core of the micelles is still loaded with the metal precursor rather than with a metal. In order to obtain regularly arranged naked metal nanodots on top of the substrate, additional steps are necessary. Physical and chemical reducing methods of particle formation are investigated (see Scheme 1). The physical method involves the use of O_2 plasma (Diener RF Plasma, Femto 3, 13.56 MHz, 50 W, p_{O_2} = 0.25 mbar) to reduce the metal precursors to a metal and remove the polymer matrix. In the chemical method, the hydrazine (N_2H_4) reducing agent is used to form the metallic particle. Two different chemical approaches, named "route 1" and "route 2" are investigated. Route 1 uses hydrazine monohydrate solution. Under vigorous stirring, the hydrazine solution is quickly added to the micellar solution in toluene. This solution is then dip-coated on the Si substrate. The excess hydrazine is neutralized with hydrochloric acid directly after reduction. Route 2 uses N_2H_4 vapour as a reducing agent. Here, the Si substrates dip-coated with a monolayer of metallic salts loaded PS_{410}-*b*-$P4VP_{62}$ micelles is exposed to N_2H_4 vapour for varying lengths of time.

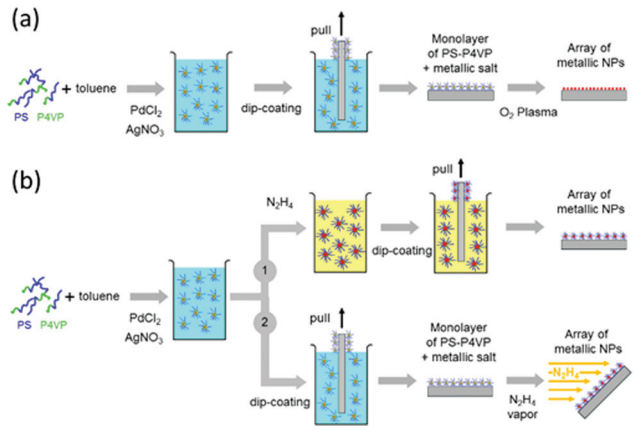

Scheme 1 Illustration of the basic steps of two methods for the formation of metallic particles: first, metal–salt precursor loaded reverse micelles are formed from PS-*b*-P4VP diblock copolymers after dissolution in toluene and addition of precursors into the solution (a) particle formation by O_2 plasma treatment or (b) particle formation by N_2H_4 reduction in solution (route 1) or under vapour after transfer of the loaded micelles onto a substrate by dip-coating (route 2).

Characterization

The nanostructures were characterized by atomic force microscopy (AFM), transmission electron microscopy (TEM), X-ray photoelectron spectroscopy (XPS) and UV-visible spectroscopy. The AFM used in this study is an upgrade Nanoscope III (Digital Instruments/Bruker) using commercially available Si cantilevers, operating in the tapping mode under ambient conditions. XPS (Kratos Analytical, Axis-Ultra) is performed using monochromatic Al Kα X-rays with a photon energy of 1486.6 eV. The pass energy of the analyzer is set at 20 eV for high-resolution spectra. The spectra are analyzed using CasaXPS v.2.3.15 software. The Si 2p peak is used as the reference for binding energy calibration. Quantitative elemental compositions are determined from peak areas using experimentally determined sensitivity factors and the spectrometer transmission function. TEM is performed using two microscopes: (i) a JEOL JEM 2010 operating at 200 kV and equipped with a UHR pole-piece (0.196 nm point resolution) and Pentafet-LinK Si(Li) EDX spectrometer (Oxford Instruments), (ii) a FEI Titan G2 80–300 kV ETEM (0.085 nm resolution) equipped with a SDD X-MaxN 80T EDX spectrometer (Oxford Instruments) and a Gatan Imaging Filter Tridiem ERS (Gatan Instruments). To prepare the samples for TEM observation, amorphous carbon and SiO_2 coated copper grids (3.05 mm, 200 mesh) are used as substrates for dip coating the micelle containing metallic ions. The grid is dipped into a micellar solution followed by pulling out the grid with a velocity of 40 mm min^{-1}. The covered grids are dried by exposure to air. Absorption measurements are carried out on a UV 160-A Shimadzu spectrophotometer. The spectra are recorded at room temperature using 1 × 1 cm^2 quartz cuvettes when the micellar solution is investigated and using glass slides when a thick film of PS-*b*-P4VP micelles with the metallic salts is formed by dip-coating.

Results and discussion

Morphological and structural characterization

Fig. 1 displays representative large scale tapping mode AFM images (1 × 1 μm^2) of the micellar solution dip-coated on Si substrates after various reduction treatments such as O_2 plasma treatment or hydrazine reduction treatments (see Scheme 1). For all images, sharp AFM tips (tip radius <7 nm) are used to minimize the tip broadening effect. Fig. 1 shows that the micelles preferentially arrange themselves in a quasi-hexagonal pattern of nanodots. After the plasma treatment, the organic compounds are removed from the micelles while the hexagonal pattern is maintained (Fig. 1c). Note that the experimental evidence of polymer removal is provided by XPS based on the C 1s spectra (not shown here) and HRTEM obser-

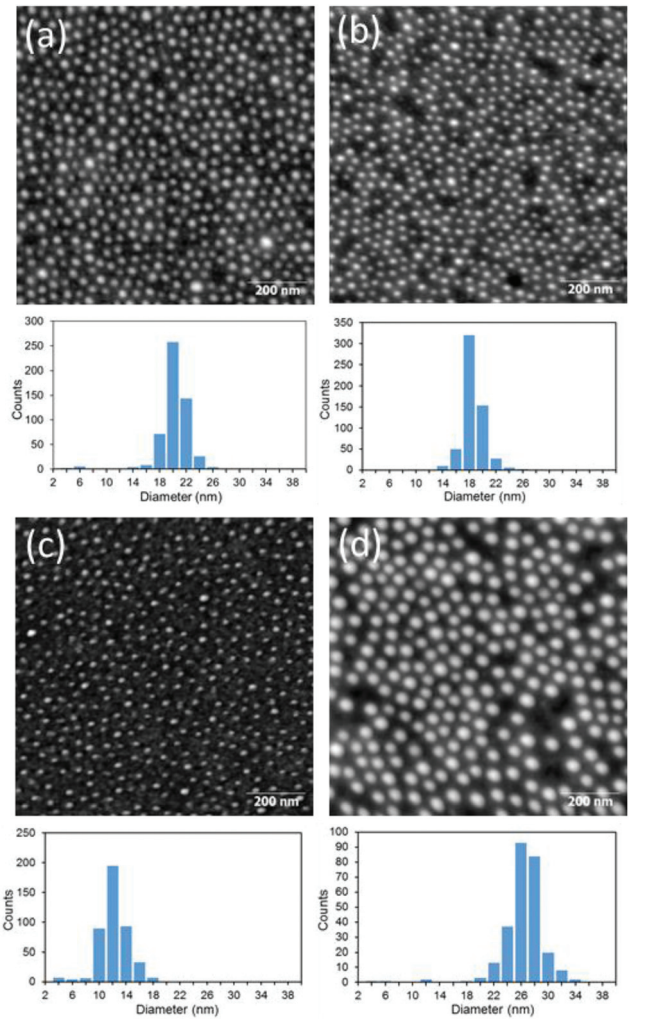

Fig. 1 Two-dimensional tapping mode AFM images (1 × 1 μm^2) and particle size distributions (lower panels) of ordered array on a silicon substrate of (a) PS_{410}-*b*-$P4VP_{62}$ micelle without metallic salt loading the micellar core, (b) containing $PdCl_2$ and $AgNO_3$ salts, (c) same preparation as in (b) but after 5 min O_2 plasma treatment and (d) same preparation as in (b) but after N_2H_4 reduction in solution. For all samples, the Pd and Ag salt loading is equivalent (R: loading ratio Pd/N and Ag/N of 0.2).

vations (see below). The location and order of the nanodots correspond to the original pattern of Fig. 1a. The average center–center nanodot distance does not change (about 55 nm). The average size reduces from 19 ± 2 nm (before O_2 plasma: see Fig. 1b) to roughly 12 nm ± 1 nm (after the O_2 plasma: see Fig. 1c). Fig. 1d shows the surface morphology of a monolayer film obtained after dip-coating of the $PdCl_2$ and $AgNO_3$ salts micellar solution reduced by N_2H_4 under strong stirring for 24 h (route 1). The ordered structure of nanodots is maintained with a higher average diameter of roughly 26 nm ± 2 nm due to the swelling of the P4VP core in the presence of N_2H_4. However, the tapping mode AFM observations here cannot determine whether the $PdCl_2$ and $AgNO_3$ salts embedded in the P4VP core are aggregated *in situ* and reduced to metallic NPs by N_2H_4 or not. The particle size histogram calculated from the AFM image of Fig. 1d also shows a broadening of the nanodot size distribution. Note that similar observations are reported when the salt loaded micellar monolayer is subjected to reduction by exposure to N_2H_4 vapour (route 2). To summarize, the AFM images demonstrate the validity of our preparation method for the synthesis of bimetallic catalysts with narrow size distributions.

To gain more insight about the morphology and internal particle structure, TEM experiments are carried out. Fig. 2 shows TEM micrographs of monofilms of $AgNO_3$ and $PdCl_2$ salt loaded PS_{410}-*b*-$P4VP_{62}$ micelles deposited by dip-coating

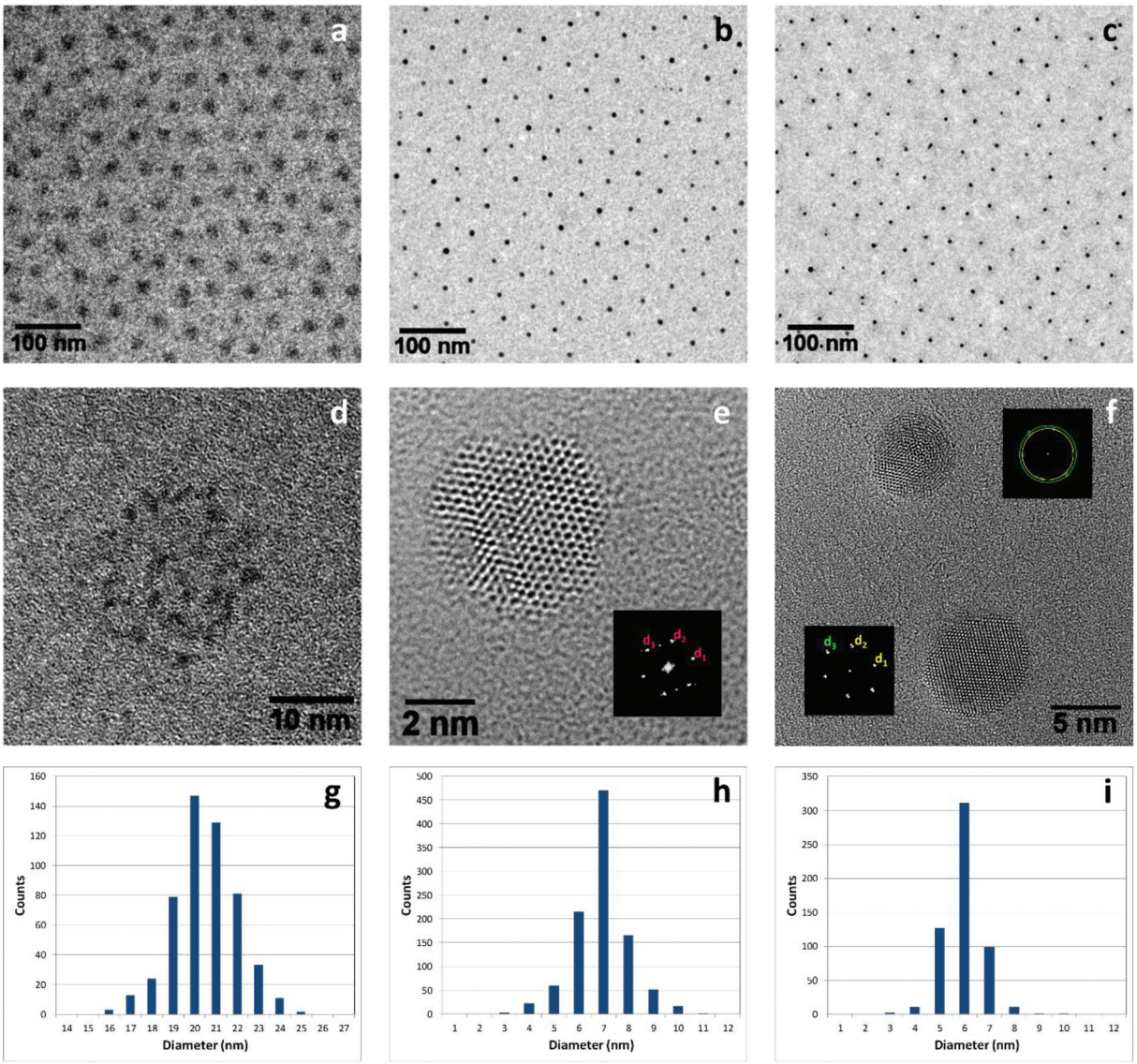

Fig. 2 Representative TEM (a–c) and HRTEM (d–f) images and size-histograms (g–i) for PS_{410}-*b*-$P4VP_{62}$ micelle containing $PdCl_2$ and $AgNO_3$ salts before (a, d, g) and after reduction by O_2-plasma treatment (b, e, h) and N_2H_4 reduction in solution (c, f, i). 2D-FFTs for each NP are inserted in the HRTEM images (e, f) for the two reduced samples. For all samples, the Pd and Ag salt loading is equivalent (loading ratio Pd/N and Ag/N of 0.2). The monofilms are cast from solution on a carbon-coated copper grid as in (a, d) and (c, f) or on a SiO_2-coated copper grid as in (b, e).

on a carbon and/or SiO_2-coated copper grid before and after O_2 plasma and N_2H_4 reducing agent treatments. The TEM images of $AgNO_3$ and $PdCl_2$ salt loaded micelle monofilm in Fig. 2a and d shows that the metallic loaded micelles preferentially arrange to form a quasi-hexagonal pattern on the carbon coated copper grid. Close observation of the P4VP cores (Fig. 2d) revealed a fine grain substructure inside every micelle corresponding to ultrasmall PdAg particles. Their formation could be explained by the electron irradiation effects instantaneously reducing the metallic salts since their contrast is enhanced when the electron beam exposure time increases. The average diameter of the micelles is estimated by TEM to be 20 ± 2 nm in reasonable agreement with the AFM. The center to center distance of the spherical micelles is, on average, 60 nm. This distance is defined by the shell of PS, which is not visible in the TEM because of its small electron density.

Fig. 2b and e show TEM images of a monofilm of $PdCl_2$- and $AgNO_3$-loaded PS_{410}-*b*-$P4VP_{62}$ micelles after 2 min of O_2 plasma exposure. The polymer matrix is completely removed (no residual carbon around NPs) and a hexagonal pattern of nanodots matching that observed before the plasma treatment is clearly visible. Fig. 2h shows the size distribution of the NPs as obtained by TEM observations. The average particle diameter is 7 nm. Over this range of particle sizes (<20 nm), there is a significant difference between the AFM and TEM particle sizes measured by AFM and by TEM due to the space convolution of the particle with the AFM tip which increases the lateral dimensions as is often observed for supported nanoparticles.[31–35] The presence of residual carbon layer around the nanoparticle that could overestimate the values in AFM measurements is ruled out since the TEM observations clearly show NPs with very clean surfaces without a trace of residual carbon around them (see Fig. 2e and f). Previous work has shown that the TEMs used for our observations allow imaging of organic nanometer layers.[36]

Fig. 2e shows an HRTEM image of a representative PdAg NP with its 2D-FFT as an insert. All the NPs appear to be crystalline and most of them are twinned like the one in Fig. 2e. The measurement of the interplanar *d*-spacings and angles clearly indicates that the zone-axis corresponding to the orientation of the NP is close to a ⟨111⟩ type zone-axis. Indeed, the measured angles are approximately 60° and the *d*-spacings correspond to {110} type planes. A comparison between the measured *d*-spacings and those reported in the literature[37] for PdAg alloys with fcc structure parameters intermediate to Pd and Ag (see Table 1) suggests that the NPs formed after 2 min O_2 plasma are Pd-rich PdAg alloys with fcc structures. The small deviation between the measured and reported values is within the experimental error of our measurement technique. A clear indication of alloy particle formation is given by the presence of {110}-type spots in the 2D-FFT (see insert in Fig. 2e and Table 1). Such spots should be absent for pure Ag and Pd NPs (all atoms have the same atomic form factor in the lattice) but present for PdAg alloy NPs (different atomic form factors in the lattice) owing to the extinction rules for fcc structures. In addition, single-particle EDX analysis performed on about 50 NPs confirmed that all NPs contained both metals, Pd and Ag, with an average Pd/Ag atomic ratio of 0.77 ± 0.06 which is consistent with the Pd-rich PdAg alloy observed by HRTEM.

Fig. 2c and f shows representative TEM images of a monofilm of $AgNO_3$ and $PdCl_2$ salt loaded PS-*b*-P4VP micelles after reduction with N_2H_4, clearly revealing particles embedded in the P4VP core of the micelles. The TEM image shows spherical shape particles with an average diameter of about 6 nm and a very narrow size distribution (see Fig. 2i). Here, direct comparison between AFM and TEM particle size distribution does not make sense since only the P4VP core can be imaged by AFM measurement.

HRTEM images and corresponding 2D-FFTs of two representative NPs are shown in Fig. 2f. The HRTEM image and 2D-FFT of the smaller particle (see the top of Fig. 2f) indicate that this particle is polycrystalline. 2D-FFT clearly shows features related to diffraction Debye–Scherrer rings assigned to

Table 1 Measured interplanar *d*-spacings and angles corresponding to the 2D-FFTs inserted in Fig. 2e and f (bottom) together with the theoretical values for the same parameters in Pd, Ag, PdAg and Pd_9Ag fcc structures. The latter are taken from the ICSD[37]

	Interplanar distance type	Measured distance (±0.020 nm)	Reported value for Pd ICSD #52251	Reported value for Ag ICSD #52257	Reported value for PdAg ICSD #181301	Reported value for Pd_9Ag ICSD #605664	Measured angle (±1°)	Reported angle for FCC structure
NP in Fig. 2e								
d_1	$d_{(110)}$	0.267 nm	Extinction	Extinction	0.2812 nm	0.2766 nm	—	—
d_2	$d_{(011)}$	0.262 nm	Extinction	Extinction	0.2812 nm	0.2766 nm	—	—
d_3	$d_{(-101)}$	0.262 nm	Extinction	Extinction	0.2812 nm	0.2766 nm	—	—
Angle $[pl_1,pl_2]$	—	—	—	—	—	—	61.0°	60.00°
Angle $[pl_2,pl_3]$	—	—	—	—	—	—	119.2°	120.00°
NP in Fig. 2f **(bottom)**								
d_1	$d_{(111)}$	0.229 nm	0.2246 nm	0.2359 nm	0.2296 nm	0.2258 nm	—	—
d_2	$d_{(111)}$	0.231 nm	0.2246 nm	0.2359 nm	0.2296 nm	0.2258 nm	—	—
d_3	$d_{(002)}$	0.199 nm	0.1945 nm	0.2044 nm	0.1989 nm	0.1956 nm	—	—
Angle $[pl_1,pl_2]$	—	—	—	—	—	—	70.9°	70.53°
Angle $[pl_2,pl_3]$	—	—	—	—	—	—	55.1°	54.74°

(111) and (002) type planes, which are typical for a face-centered cubic (fcc) crystal lattice and confirms that this particle is metallic (cubic oxide phases of Pd and Ag do not have lattice parameters consistent with the measured ones).[37] The positions of the rings are both intermediate between those corresponding to the pure Ag and Pd metals, which is an indication of the formation of NPs of mixed composition. For the bigger particle at the bottom of Fig. 2f, the HRTEM image and 2D-FFT clearly show that this particle is highly single crystalline. The measured interplanar *d*-spacings and angles and the reported data for pure Ag, Pd and PdAg alloys with fcc crystal structures (see Table 1) suggest that this particle is a metallic Pd-rich PdAg alloy nanocrystal oriented in the [1−10] direction. The single-particle EDX analysis also confirmed that all particles contained both Pd and Ag metals. An average Pd/Ag atomic ratio of 0.71 ± 0.04 is estimated, which is very similar to that obtained with the monofilm treated with O_2 plasma.

The single-particle EDX analysis based on a randomly chosen collection of NPs shows that the average composition of the PdAg NPS after O_2 plasma or reduction under hydrazine deviates significantly from the initial composition which corresponds to the Pd/Ag ratio of the salt initially loaded in the micellar core. This deviation suggests that the $AgNO_3$ salt is partially embedded in the micellar core mainly due to its solubility in toluene being substantially lower than that of the $PdCl_2$ salt. This is verified by our TEM observations showing $AgNO_3$ crystals present on the surface. It is important to note that when single particle EDX is performed within the AgPd particle arrays, a high electron fluence results in a higher Pd/Ag atomic measured ratio (loss of Ag atoms under electron beam). Great care has therefore been taken to work under low dose conditions to minimize sample degradation to reflect the true composition of the particles. Our previous works have shown that the optimal solution to obtain a good quantification by EDX of the composition of bimetallic nanoparticles even in very diluted alloys is a compromise between the acquisition time and stability of the bimetallic nanoparticles under the electron beam.[38–41] The EDX analysis also revealed that the samples treated with O_2 plasma induce a higher inhomogeneity of the Pd/Ag ratio. The O_2 plasma is used to remove the organic matrix and generate the bimetallic nanoparticles. However the plasma process is hard to understand and occurs through a combination of sputtering, electron-induced reactions and etching with free radicals which depends on the NPs structure and composition.[42,43]

Electronic and chemical characterization

In order to better understand the interaction between the metal salt and the copolymer micellar core, XPS measurements are performed on $PdCl_2$- and $AgNO_3$-loaded PS_{410}-*b*-$P4VP_{62}$ micelles (loading ratio: $R = 0.4$) to study the chemical interplay between the involved species. In the P4VP core, the nitrogen atom of the pyridine group can act as σ-donor and π-acceptor ligand and can coordinate with the metals through covalent bonding.[44] Evidence for the bonding of the metal ions to the copolymer can be seen by comparing the N 1s XPS spectra in Fig. 3-1 before and after the incorporation of metal salts. The N 1s spectrum of the unloaded PS_{410}-*b*-$P4VP_{62}$ shows only one binding state of the nitrogen atoms at 399.5 eV (Fig. 3-1(a)) in agreement with the literature.[45,46] As expected, the loading of the PS_{410}-*b*-$P4VP_{62}$ core with palladium or/and silver ions changes the binding energy of the corresponding N 1s spectrum (Fig. 3-1(b and d)). Thus, a new highly energetic N 1s peak is observed for both metallic salts around 401.2 eV and 400.7 eV for $PdCl_2$- and $AgNO_3$-loaded PS_{410}-*b*-$P4VP_{62}$ core respectively. It is assumed that this component peak shows nitrogen, which is involved in a complex formation with salt ions. The binding energy of nitrogen is governed by the charge transfer of the electron lone pair from the sp^2 nitrogen orbital to the electron-accepting orbitals of the metal. However, the N 1s peak associated with the unloaded PS_{410}-*b*-$P4VP_{62}$ is still present indicating that a fraction of the pyridine nitrogen participates in the interaction with the salt metallic cations. An additional component peak appears at 407 eV for the $AgNO_3$-loaded PS_{410}-*b*-$P4VP_{62}$ samples (Fig. 3-1(c and d)). This component peak shows nitrogen, which is assigned to the N 1s transition in the nitrate ion (NO_3^-).

Fig. 3-2(a) shows the Pd 3d spectra of $PdCl_2$ after dilution in toluene and deposition into a Si sample. Similar to spectra from the literature,[47] the Pd 3d spectrum of Pd Cl_2 shows a single Pd $3d_{5/2}$ peak at binding energy of 339.8 eV. When the Pd Cl_2 loaded the P4VP core, the Pd 3d spectrum (Fig. 3-2(b)) shows a Pd $3d_{5/2}$ peak at binding energy of 339.2 eV. This result shows that the binding energy of Pd in $PdCl_2$ loaded in the PS_{410}-*b*-$P4VP_{62}$ is quite similar to $PdCl_2$ alone and implies a Pd^{2+} oxidation state. Similar results are obtained for $AgNO_3$-loaded PS_{410}-*b*-$P4VP_{62}$ micelles deposited on the SiO_2/Si (100) sample. In Fig. 3-3(b and f) the peak binding energy of Ag $3d_{5/2}$ at 369 eV is significantly higher than the expected value for bulk Ag^0 (368.0 eV) and the measured value (368.3 eV) for Ag in $AgNO_3$ in Fig. 3-3(a). These results are in agreement with the peak energy values reported previously[48] and suggest that the Ag^{1+} ions of the $AgNO_3$ salt are coordinated to the pyridyl groups of the P4VP polymer. In summary, the above results confirm that the Pd and Ag salts in the presence or not of the second metal are successfully loaded in the micellar core and a coordination interaction between metal atoms and pyridine is involved.

XPS is also used to gain some insight on the particle formation processes by means of plasma treatment or hydrazine reduction. Pd 3d and Ag 3d spectra after the different processes were measured for $PdCl_2$- and $AgNO_3$-loaded PS_{410}-*b*-$P4VP_{62}$ micelles. The Pd 3d spectra are shown in Fig. 3-2. When the P4VP micelle cores are loaded with only the $PdCl_2$ salt, the Pd 3d spectrum (Fig. 3-2(c)) obtained after 2 min O_2 plasma exposure time shows a single peak for Pd $3d_{5/2}$ at 335.3 eV. This agrees well with the peak positions assigned in the literature to the reduced metallic Pd^0.[49,50] When the O_2 plasma exposure time is increased up to 5 min, the binding energy of Pd 3d shifts to 336.9 eV (Fig. 3-2(d)) which are assigned to the Pd^{2+} oxide (*i.e.* PdO).[51,52] A trace of metallic Pd is still observed. After treatment under H_2 pressure at 400 °C for 1 h

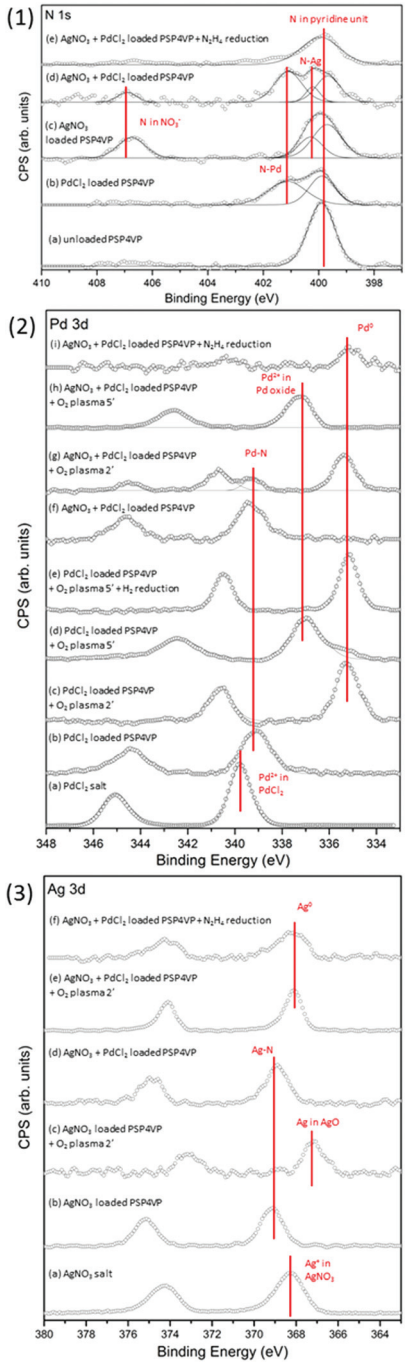

Fig. 3 (1) N 1s, (2) Pd 3d and (3) Ag 3d XPS spectra of PS_{410}–PVP_{62} micelle monolayer on silicon substrate with or without $PdCl_2$ and/or $AgNO_3$ salt loading the micellar core and after different treatments. For all samples, the Pd and Ag salt loading is equivalent (R: loading ratio Pd/N and Ag/N of 0.2).

of the 5 min O_2 plasma sample, the reduction of Pd^{2+} to Pd^0 (peak at 335.3 eV) is clearly observed in the Pd $3d_{5/2}$ spectra of the Fig. 3-2(e). Similar results are obtained when the P4VP micelle cores are loaded with both Ag and Pd salts (Fig. 3-2(g and h)). Fig. 3-3 also shows Ag 3d spectra after plasma treatment and hydrazine reduction treatment. Although the shift in binding energy between the Ag^+ and Ag^{2+} states in silver oxides and the Ag^0 metallic state is rather small,[53,54] the binding energy of $Ag_{5/2}$ at 367.3 eV, after 2 min O_2 plasma into $AgNO_3$ loaded PS_{410}-*b*-$P4VP_{62}$ micelles, suggests a complete oxidation of Ag atoms to AgO.

It is interesting to note that when samples with both $PdCl_2$ and $AgNO_3$ embedded inside the PS_{410}-*b*-$P4VP_{62}$ core are exposed for 2 min to O_2 plasma, the Ag $3d_{5/2}$ XPS peak is found at 368.0 eV which can be ascribed to the metallic Ag^0 state. The XPS results reveal that the formation of nanoparticles is practically accomplished after 2 min of oxygen plasma exposure. The nanoparticles are in a metallic state after such a treatment in agreement with the TEM investigations. However, when the O_2 plasma exposure time is increased, an oxidation of nanoparticles is observed. Fig. 3-1(e), 2(i) and 3(i) show respectively the N 1s, Pd 3d and Ag 3d XPS spectra of $PdCl_2$- and $AgNO_3$-loaded PS_{410}-*b*-$P4VP_{62}$ micelles after hydrazine treatment. The XPS results suggest that the PS_{410}-*b*-$P4VP_{62}$ micelles are still present as indicated by the N 1s peak and that the nanoparticles formed by salt reduction under N_2H_4 are in a metallic state (see Pd 3d and Ag 3d peaks, Fig. 3).

UV-Vis spectral analysis of the salt reduction under hydrazine

As described before, an alternative method to plasma for obtaining metallic nanoparticles in the core volume of the micelle is to reduce the immobilized Ag and/or Pd salts by N_2H_4. Two approaches using N_2H_4 as a reducing agent have been investigated: the first is the addition of N_2H_4 liquid in the salt loaded copolymer dissolved in toluene and the second is the exposure of a metallic salt loaded micellar film to N_2H_4 vapour. The formation of metal nanoparticles is detected by UV-Vis spectroscopy. As each metal nanoparticle has its own characteristic localized surface plasmon resonance (LSPR) band, valuable information is provided on the nature and stability of the metal nanoparticles. The time dependence of the formation of NPs is monitored by UV-visible absorption spectroscopy as illustrated in Fig. 4. Fig. 4a and 4b show the time dependent absorption spectra of $AgNO_3$ loaded PS_{410}-*b*-$P4VP_{62}$ micelles using both N_2H_4 reducing processes. When route 1 was used (Fig. 4a), approximately 6 min after the addition of N_2H_4, the color of the solution was faint yellow and displayed a diffuse LSPR peak at 433 nm, which can be attributed to the formation of small Ag nanocrystals.[55–57] Over the next 40 min, the LSPR peak amplitude increases rapidly with a slight blue shift reaching a maximum at 419 nm followed by a monotonic red shift up to 426 nm over the remaining 24 h. This blue shift can be explained by two different effects: (i) the change in the dielectric medium within the $AgNO_3$ loaded P4VP cores when N_2H_4 diffuses within the cores and swells them as observed in the AFM images and (ii) a reduction in the size dispersity of the nanoparticles as previously reported for the formation of trioctylamine-stabilized spherical silver nanoparticles.[58] When route 2 is used, the absorption spectra (Fig. 4b) of the $AgNO_3$ loaded PS_{410}-*b*-$P4VP_{62}$ micelle films quickly (10 s in N_2H_4 vapour) show a broad and blue-shifted asymmetric surface plasmon absorp-

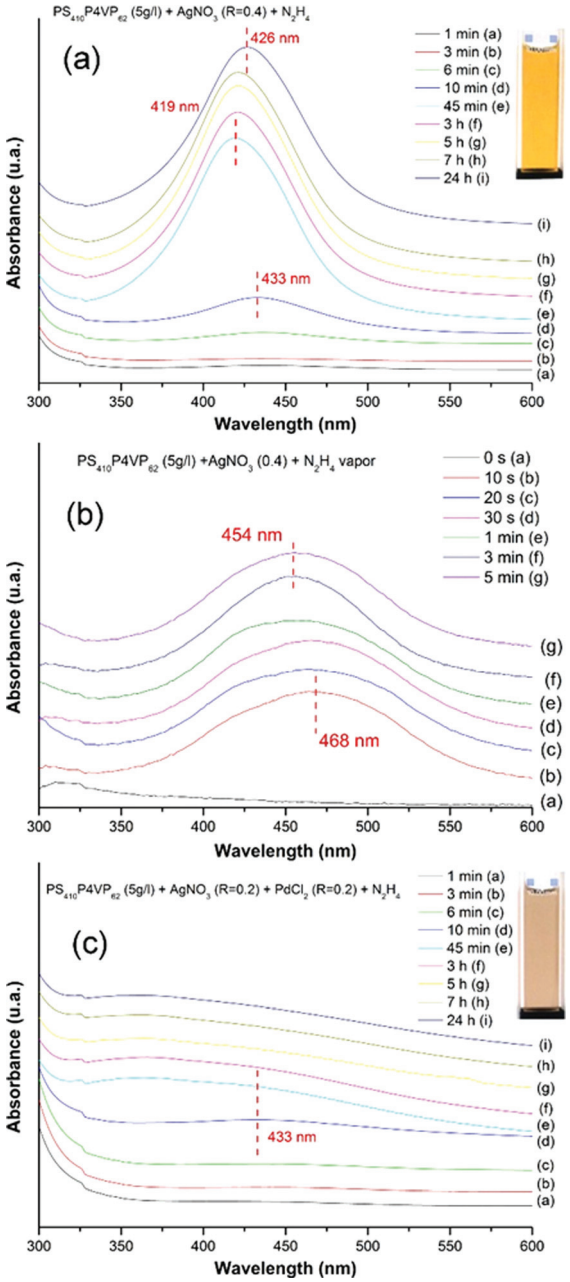

Fig. 4 UV-vis spectra at different reduction times of (a) PS_{410}-*b*-$P4VP_{62}$ micelles containing $AgNO_3$ after the addition N_2H_4 liquid (route 1), (b) PS_{410}-*b*-$P4VP_{62}$ micelles containing $AgNO_3$ under N_2H_4 vapour (route 2), (c) PS_{410}-*b*-$P4VP_{62}$ micelles containing $PdCl_2$ and $AgNO_3$ after the addition N_2H_4 liquid (route 1). In the insert of (a) and (c), photographs of Ag and PdAg NPs dispersions in toluene obtained 24 h after the addition of N_2H_4 solution.

tion band with a maximum at 468 nm. These LSPR peaks become narrower and more symmetrical when the exposure time is increased with a maximum at 454 nm. The asymmetry of the LSPR peak could be attributed to an asymmetry of the size distribution of the Ag NPs inside the P4VP core during the early stage of NP formation. Fig. 4c shows the time dependent absorption spectra of the co-reduction of $AgNO_3$ and $PdCl_2$ salts embedded in the P4VP core with N_2H_4 in solution (route 1). A broad absorption band over the entire visible range is observed whereas the colorless micellar solution turned pale brown with the addition of hydrazine solution. It is clear that the presence of Pd strongly affects the LSPR of Ag NPs. Similar observations have been reported for mixed NPs studied at different Pd/Ag ratios.[59,60] The characteristic LSPR bands of Fig. 4 suggest that the particles formed by salt reduction under hydrazine are metallic and when both $AgNO_3$ and $PdCl_2$ salts are used, bimetallic PdAg particles generated in the P4VP core are alloy particles ruling out the presence of isolated Ag particles. It can be noted that the solutions are stable at room temperature and can be stored in a transparent vial for as long as several weeks or months.

Conclusion

We have demonstrated that well-ordered arrays of bimetallic PdAg nanoparticles can be produced using a PS-*b*-P4VP block copolymer template. Each step of the process of nanoparticle formation has been characterized by AFM, TEM, XPS and UV-visible spectroscopy. AFM, TEM and EDX show that an ordered array of micelle monolayers containing $PdCl_2$ and $AgNO_3$ salts can be made by a dip coating process, with a well-defined interparticle distance and a narrow distribution of size and composition. XPS spectra confirm that the $PdCl_2$ and $AgNO_3$ salts in the presence or not of the second metal are successfully loaded in the micellar core and a coordination interaction between metal atoms and pyridine is involved. At this stage, the core of the micelles is still loaded with the metal precursor rather than with a metal. In this study, we show that various reducing methods (physical reduction by O_2 plasma, chemical reduction by hydrazine solution and vapour) can be used to synthesize PdAg nanoparticles. AFM and TEM observations show that the ordered array of nanodots is not altered by the reducing process. PdAg nanoparticles with average diameters of about 6–7 nm are obtained. HRTEM and EDX indicate that Pd-rich PdAg alloy nanoparticles are synthesized by chemical or physical reduction. UV-visible spectroscopy observations confirm that bimetallic PdAg nanoparticles are quickly formed after chemical reduction. XPS measurements reveal the metallic state in the PdAg alloy nanoparticles after 2 min of O_2 plasma and hydrazine reduction. However, when the O_2 plasma exposure time is increased, the XPS spectra suggest an oxidation of the PdAg nanoparticles. The synthesis of such bimetallic particles with good control over the composition, particle size, shape and interparticle spacing makes these surfaces ideally suited for model study in catalysis to understand and control their catalytic performance.

Acknowledgements

E. E. and F. J. C. S. A. thank CNRS for grant no. 98087 within the Franco-Siberian Center; G. V. M. and T. A. B. acknowledge

the Tomsk State University Academic D. I. Mendeleev Fund Program. I. A. Kurzina is gratefully acknowledged for helpful discussions regarding PdAg catalysts. Thanks to A. Oprisor and M. Lazare for technical support on the polymer synthesis.

Notes and references

1 T. Smart, H. Lomas, M. Massignani, M. V. Flores-Merino, L. R. Perez and G. Battaglia, *Nano Today*, 2008, **3**, 38.
2 S. B. Darling, *Prog. Polym. Sci.*, 2007, **32**, 1152.
3 L. Leibler, *Macromolecules*, 1980, **13**, 1602.
4 H.-A. Klok and S. Lecommandoux, *Adv. Mater.*, 2001, **13**, 1217.
5 A.-V. Ruzette and L. Leibler, *Nat. Mater.*, 2005, **4**, 19.
6 W. Wen, W. Zhang, G. Wie, Y. Wang, J. Zhang, M. Zhang and L. Shi, *Chem. Mater.*, 2008, **20**, 2144.
7 J. Kim, J. Bang, C. J. Hawker and E. J. Kramer, *Macromolecules*, 2006, **39**, 4108.
8 A. W. Fahmi and M. Stamm, *Langmuir*, 2005, **21**, 1062.
9 K. K. Tenneti, X. Chen, C. Y. Li, X. Wan, X. Fan, Q. F. Zhou, L. Rong and B. S. Hsiao, *Macromolecules*, 2007, **40**, 5095.
10 Y. Suzuki, H. Nishide and E. Tsuchida, *Macromolecules*, 2000, **33**, 2530.
11 I. W. Hamley, *Developments in Block Copolymer Science and Technology*, John Wiley and Sons, 2004, p. 380.
12 R. P. Zhu, Y. M. Wang and W. D. He, *Eur. Polym. J.*, 2005, **41**, 2088.
13 J. T. Zhu, H. Z. Yu and W. Jiang, *Macromolecules*, 2005, **38**, 7492.
14 J. Ruokolainen, G. ten Brinke and O. Ikkala, *Adv. Mater.*, 1999, **11**, 777.
15 O. Ikkala and G. ten Brinke, *Science*, 2002, **295**, 2407.
16 O. Ikkala and G. ten Brinke, *Chem. Commun.*, 2004, 2131.
17 Z. Gao, S. K. Varshney, S. Wong and A. Eisenberg, *Macromolecules*, 1994, **27**, 7923.
18 H. Shen, L. Zhang and A. Eisenberg, *J. Am. Chem. Soc.*, 1999, **121**, 2728.
19 X. Yang, B. A. Moosa, L. Deng, L. Zhao and N. M. Khashab, *Polym. Chem.*, 2011, **2**, 2543.
20 S. Park, B. Kim, O. Yavuzcetin, M. T. Tuominen and T. P. Russell, *ACS Nano*, 2008, **2**, 1363.
21 H.-C. Kim, S.-M. Park and W. D. Hinsberg, *Chem. Rev.*, 2010, **110**, 146.
22 L. Bronstein, M. Antonietti and P. Valetsky, in *Nanoparticles and Nanostructured Films*, ed. J. H. Fendler, Wiley, 1998, p. 145.
23 J. P. Spatz, S. Mössmer, C. Hartmann, M. Möller, T. Herzog, M. Krieger, H.-G. Boyen, P. Ziemann and B. Kabius, *Langmuir*, 2000, **16**, 407.
24 E. B. Gowd, B. Nandan, N. C. Bigall, A. Eychmüller, P. Formanek and M. Stamm, *Polymer*, 2010, **51**, 2661.
25 K. Mikkelsen, B. Cassidy, N. Hofstetter, L. Bergquist, A. Taylor and D. A. Rider, *Chem. Mater.*, 2014, **26**, 6928.
26 G. Cé Guinto, E. Beyou and E. Bourgeat-Lami, *J. Polym. Sci., Part A: Polym. Chem.*, 2010, **48**, 784.
27 J. P. Spatz, S. Mössmer, M. Moller, T. Herzog, A. Plettl and P. Ziemann, *J. Lumin.*, 1998, **76–77**, 168.
28 J. Lu, S. S. Yi, T. Kopley, C. Qian, J. Liu and E. Gulari, *J. Phys. Chem. B*, 2006, **110**, 6659.
29 C.-A. Dai, Y.-L. Wu, Y.-H. Lee, C.-J. Chang and W.-F. Su, *J. Cryst. Growth*, 2006, **288**, 128.
30 M. Xiong, K. Zhang and Y. Chen, *Eur. Polym. J.*, 2008, **44**, 3835.
31 S. K. Shaikhutdinov and F. J. Cadete Santos Aires, *Langmuir*, 1998, **14**, 3501.
32 L. Lianos, A. Berthet, C. Deranlot, F. J. Cadete Santos Aires, J. Massardier and J. C. Bertolini, *J. Catal.*, 1998, **177**, 129.
33 P. Kéghélian, P. Mélinon, A. Perez, J. Lermé, C. Ray, M. Pellarin, M. Broyer, J. L. Rousset and F. J. Cadete Santos Aires, *Eur. Phys. J. D*, 1999, **9**, 639.
34 P. Mélinon, P. Kéghélian, J. L. Rousset, A. M. Cadrot, A. Malhomme, A. J. Renouprez and F. J. Cadete Santos Aires, *Philos. Mag. A*, 2000, **89**, 143.
35 A. Berthet, A. L. Thomann, F. J. Cadete Santos Aires, M. Brun, C. Deranlot, J. C. Bertolini, J. P. Rozenbaum, P. Brault and P. Andreazza, *J. Catal.*, 2000, **190**, 49.
36 T. Caillot, G. Gauthier, P. Delichère, C. Cayron and F. J. Cadete Santos Aires, *J. Catal.*, 2012, **290**, 158.
37 Inorganic Crystal Structure Database (Fachinformationszentrum (FIZ) Karlsruhe, Germany, and the National Institute of Standards and Technology (NIST)/U.S. Department of Commerce on the behalf of the United States).
38 J. L. Rousset, A. M. Cadrot, F. J. Cadete Santos Aires, A. Renouprez, P. Mélinon, A. Perez, M. Pellarin, J. L. Vialle and M. Broyer, *J. Chem. Phys.*, 1995, **102**, 8574.
39 J. L. Rousset, F. J. Cadete Santos Aires, B. R. Sekhar, P. Mélinon, B. Prevel and M. Pellarin, *J. Phys. Chem. B*, 2000, **104**, 5430.
40 R. Mahfouz, F. J. Cadete Santos Aires, A. Brenier, E. Ehret, M. Roumié, B. NSouli, B. Jacquier and J. C. Bertolini, *J. Nanopart. Res.*, 2010, **12**, 3123.
41 K. Pattamakomsan, E. Ehret, F. Morfin, P. Gélin, Y. Jugnet, S. Prakash, J. C. Bertolini, J. Panpranot and F. J. Cadete Santos Aires, *Catal. Today*, 2011, **164**, 28.
42 F. D. Egitto, *Pure Appl. Chem.*, 1990, **62**, 1699.
43 M. Song, Q. Wang, X. Zuo and Y. Meng, *ECS Solid State Lett.*, 2012, **1**, M16.
44 M. Koenig, F. Simon, P. Formanek, M. Müller, S. Gupta, M. Stamm and P. Uhlmann, *Macromol. Chem. Phys.*, 2013, **214**, 2301.
45 H. T. Oyama and T. Nakajima, *J. Appl. Polym. Sci.*, 1984, **29**, 2143.
46 A. K. Zharmagambetova, V. A. Golodov and Y. P. Saltykov, *J. Mol. Catal.*, 1989, **55**, 406.
47 W. Lee, S. Y. Lee, X. Zhang, O. Rabin and R. M. Briber, *Nanotechnol.*, 2013, **24**, 045305.
48 M. Aizawa and J. M. Buriak, *Chem. Mater.*, 2007, **19**, 5090.
49 M. G. Mason, *Phys. Rev. B: Condens. Matter*, 1983, **27**, 748.
50 G. K. Wertheim and S. B. DiCenzo, *Phys. Rev. B: Condens. Matter*, 1988, **37**, 844.
51 T. Pillo, R. Zimmermann, P. Steiner and S. J. Hufner, *Phys. Condens. Matter*, 1997, **9**, 3987.
52 L. S. Kibis, A. I. Stadnichenko, S. V. Koscheev, V. I. Zaikovskii and A. I. Boronin, *J. Phys. Chem. C*, 2012, **116**, 19342.

53 V. K. Kaushik, *J. Electron Spectrosc. Relat. Phenom.*, 1991, **56**, 273.
54 A. M. Ferraria, A. P. Carapeto and A. M. Botelho do Rego, *Vacuum*, 2012, **86**, 1988.
55 S. D. Solomon, M. Bahadory, A. V. Jeyarajasingam, S. A. Rutkowsky, C. Boritz and L. Mulfinger, *J. Chem. Educ.*, 2007, **84**, 322.
56 R. Abargues, K. Abderrafi, E. Pedrueza, R. Gradess, J. Marqués-Hueso, J. L. Valdés and J. Martinez-Pastor, *New J. Chem.*, 2009, **33**, 1720.
57 W. G. Menezes, V. Zielasek, G. I. Dzhardimalieva, S. I. Pomogailo, K. Thiel, D. Wöhrle, A. Hartwigd and M. Bäumer, *Nanoscale*, 2012, **4**, 1658.
58 N. W. Dennis, B. B. Muhoberac, J. C. Newton, A. Kumbhar and R. Sardar, *Plasmonics*, 2014, **9**, 111.
59 L. D'Souza, P. Bera and S. Sampath, *J. Colloid Interface Sci.*, 2002, **246**, 92.
60 K. Patel, S. Kapoor, D. P. Dave and T. Mukherjee, *J. Chem. Sci.*, 2005, **117**, 311.